RESEARCH ARTICLE OPEN ACCESS

Numerical Modeling of MICP Grouting in Homogeneous and Layered Heterogeneous Soils

Guo-Liang Ma[1] | Zhen-Yu Yin[1,2] | Yang Xiao[3]

[1]Department of Civil and Environmental Engineering, The Hong Kong Polytechnic University, Hong Kong, China | [2]Research Centre for Nature-based Urban Infrastructure Solutions, The Hong Kong Polytechnic University, Hong Kong, China | [3]School of Civil Engineering, Chongqing University, Chongqing, China

Correspondence: Zhen-Yu Yin (zhenyu.yin@polyu.edu.hk)

ABSTRACT

Microbially induced carbonate precipitation (MICP) has been extensively studied through experiments as a potential solution for ground improvement. However, the investigation and optimization of the MICP grouting process remain incomplete due to various experimental limitations, such as budget constraints, equipment availability, time limit, and suitable sites. As a result, the numerical method could be a practical approach, providing a clearer understanding of the hydrological-biological-chemical processes involved, which could help improve the performance of MICP. In this study, a hydrological-biological-chemical coupling model was developed to simulate MICP grouting in both homogeneous and layered heterogeneous soils, which is often found in nature. The model effectively captures the impact of carbonate precipitation on critical aspects of the grouting process, such as flow field, bacterial adsorption, bacterial activity, and soil properties. Additionally, the Péclet and Damköhler numbers were introduced to comprehensively describe the impact of various grouting factors on the distribution of precipitates and the average $CaCO_3$ increment in homogeneous soils. In layered heterogeneous soils, it was observed that some solutions migrate across the interface between the two soil layers, leading to an accumulation of precipitates near the interface and forming a wedge-shaped $CaCO_3$ increment zone in the lower-permeability soil layer. Beyond this wedge-shaped zone, the distribution of $CaCO_3$ is comparable to that in homogeneous soils. These findings suggest that in layered heterogeneous soils, special attention should be given to the area adjacent to the soil interface in the less permeable layer, as the precipitate distribution in other regions mirrors that in corresponding homogeneous soils.

1 | Introduction

Microbially induced carbonate precipitation (MICP) is an innovative method that can be applied to soil stabilization, seepage control, crack repair, erosion mitigation, contaminant removal, and more [1–3]. Over the past two decades, the performance of MICP in soil stabilization has been widely studied, with a particular focus on improving soil strength and stiffness, which are typically determined by the content and distribution of $CaCO_3$ [4, 5]. The MICP technique involves injecting bacteria and chemicals, as well as urea hydrolysis and carbonate precipitation, which together form a typical advection-diffusion-reaction process [6, 7], encompassing hydraulic, physical, chemical, and biological phenomena. Specifically, bacteria and chemicals

migrated through the pore-networks of soils, a process governed by the injection strategy (e.g., one-, two-, or three-phase injection methods), injection parameters (e.g., injection velocity, bacterial concentration, and chemical concentration), and soil properties (e.g., pore structure and permeability) [8–10]. The adsorption and desorption of bacteria occur during their migration, which is typically a physical process influenced by the composition of the solution, soil properties, and settling time [11, 12]. Biomineralization, which occurs during the grouting of chemicals, is influenced by the distribution of bacteria, the concentration of chemicals, and environmental conditions, such as pH and temperature [6, 13, 14]. Finally, the formation of precipitates will, in turn, affect the hydraulic, physical, chemical, and biological processes mentioned above due to changes in porosity, pore structure, and permeability [15, 16].

The individual processes mentioned above have been widely studied through experimental work at the microscale, element scale, and field scale [17–20]. However, investigating the entire hydrological-biological-chemical process experimentally in a single study is challenging due to limitations in budget, equipment, time, and available test sites, especially for large-scale field tests. A practical solution to this issue is to develop appropriate numerical models to simulate the MICP grouting process [21, 22]. For example, hydrological-biological-chemical models have been developed to simulate the MICP grouting process in sand columns [23–25], meter-scale models [26, 27], and field-scale tests [28–30].

Although many previous simulation studies have been conducted, they typically focus on homogeneous soils [28, 31]. However, natural soils are not always homogeneous [32, 33]. For example, they may exhibit spatial variability or layered heterogeneity [32, 34, 35]. Soil heterogeneity can significantly influence the grouting process and the effectiveness of soil stabilization. For example, Zeng et al. [30] conducted MICP grouting field tests in layered heterogeneous soils, and observed that the calcium ions in effluents were detected much earlier than expected. This phenomenon was attributed to the formation of preferential flow in strata with higher permeability. Despite the frequent occurrence of layered heterogeneous soils in engineering practice, there remains a lack of comprehensive understanding regarding the performance and MICP grouting process in such conditions.

In this study, a hydrological-biological-chemical coupling model for simulating MICP grouting in homogeneous and layered heterogeneous soils was first introduced and verified. Then, we examined the influence of particle size, porosity, urease activity, and hydraulic head on the distribution of attached bacteria, $CaCO_3$ content, and $CaCO_3$ increment after each treatment cycle in homogeneous soil. The uniformity of $CaCO_3$ distribution and the stabilization efficiency, that is, $CaCO_3$ increment, were analyzed using two dimensionless parameters: the Péclet number (Pe) and the Damköhler number (Da). Next, we explored the impact of soil layering on the distribution of $CaCO_3$ considering variations in soil properties, injection parameters, and bacterial urease activity. Finally, the extent of the zone of influence (ZOI) and the increase in $CaCO_3$ content were compared with those observed in corresponding homogeneous soils.

2 | Hydrological-Biological-Chemical Coupling Model

As shown in Figure 1a, soil stabilization using the MICP technique primarily involves the migration of bacteria and chemicals, followed by the precipitation of calcite within soil pores. The physical and chemical processes include fluid flow, transport of materials, biological activities, and chemical reactions. A schematic representation of the coupling between these physical and chemical processes is provided in Figure 1b. The model is described in detail as follows.

The flow of liquids is governed by Darcy's law, assuming the soils are saturated, as is typically done for MICP cementation [36]:

$$v = -\frac{K}{\mu} \cdot (\nabla p - \rho g) \tag{1}$$

where v is the fluid velocity (m/s), K is the permeability of soils (m²), and p is the pressure (Pa). The dynamic viscosity (μ, Pa·s) and density (ρ, kg/m³) of the fluid are assumed to remain constant throughout the MICP process, in alignment with Faeli et al. [37], and Wang et al. [38]. g is the gravitational acceleration (m/s²).

The transport and fate of bacteria and chemicals are typically described by the advection-dispersion-reaction equation [39]:

$$\frac{\partial nC}{\partial t} = \nabla (nD\nabla C) - \nabla (vC) + S + R \tag{2}$$

where n is the soil porosity (dimensionless), C is the concentration of bacteria (OD) or chemicals (mol/L), t is time (s), and D is dispersion tensor composed of longitudinal and transverse dispersivity and effective diffusion (m²/s), S and R denote the bacterial activities and chemical reaction terms.

For bacteria, their growth and decay are neglected due to the relatively short reaction duration [40]. Therefore, S is the adsorption and desorption rate of bacteria. The Equation (2) is then transformed into:

$$\frac{\partial nC_{bs}}{\partial t} = \nabla (nD\nabla C_{bs}) - \nabla (vC_{bs}) - R_a + R_d \tag{3}$$

$$R_a = k_{att} \cdot n \cdot C_{bs} \tag{4}$$

$$R_d = \rho_b \cdot k_{det} \cdot C_{batt} \tag{5}$$

where C_{bs} is the concentration of suspended bacteria (OD), C_{batt} is the attached bacteria on sand surfaces ((OD·m³)/kg). R_a is the adsorption rate (OD/s), R_d is the desorption rate (OD/s), k_{att} is the attachment coefficient (s⁻¹), k_{det} is the detachment coefficient (s⁻¹), and ρ_b is the dry density of soils (kg/m³). According to filtration theory [41, 42], the attachment coefficient is given by

$$k_{att} = \frac{3(1-n)}{2d_{50}}\eta\alpha v \tag{6}$$

where d_{50} is the median diameter of sand (mm), η and α are the collector efficiency and sticking efficiency, which are the probabilities of bacteria approaching and adhesion on soil particle surfaces, respectively, and more details can be found in Rijnaarts
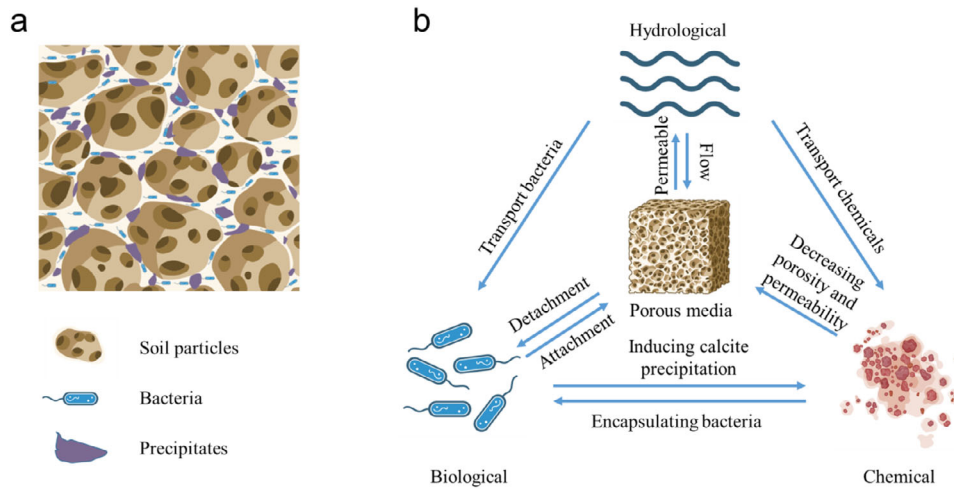
FIGURE 1 | Schematic view of (a) pore-scale MICP grouting and reaction, and (b) hydrological-biological-chemical coupling of MICP grouting (source from biorender.com).

TABLE 1 | The values of k_{att} (s^{-1}) and k_{det} (s^{-1}) at different initial particle sizes and porosities.

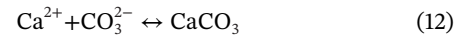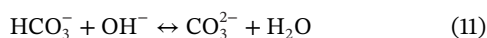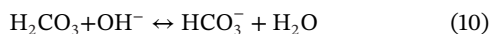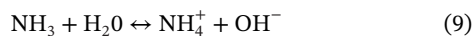| Parameters	20–30 (0.71 mm)			35–50 (0.36 mm)			70–110 (0.15 mm)		
	0.35	0.4	0.45	0.35	0.4	0.45	0.35	0.4	0.45
k_{att} (10^{-4} s^{-1})	3.35[a]	3.09	2.83	6.15[a]	5.68	5.20	12.8[a]	11.8	10.9
k_{det} (10^{-5} s^{-1})		1.77[a]			1.44[a]			1.18[a]	

[a]Data were collected from Bradford et al. [43], and the other values were calculated according to Equation (6).

et al. [41]. The influence of initial porosity and the precipitation-induced changes in porosity on the attachment coefficient can thus be calculated assuming that the variations in η and α are negligible for each soil group. The values of attachment coefficient (k_{att}) and detachment coefficient (k_{det}) for different initial particle sizes and porosities are listed in Table 1. It is assumed that the detachment coefficient remains constant for each soil group.

There is no advection and dispersion for the attached bacteria, and thus the mass conservation of the attached bacteria is described by

$$\rho_b \frac{\partial C_{batt}}{\partial t} = R_a - R_d \tag{7}$$

For chemicals, R denotes the reaction rate of chemicals. In the current work, the relevant chemical reactions include urea hydrolysis, ammonia hydration, and CaCO$_3$ precipitation, represented by the following equations:

$$CO(NH_2)_2 + 2H_2O \rightarrow 2NH_3 + H_2CO_3 \tag{8}$$

$$NH_3 + H_2O \leftrightarrow NH_4^+ + OH^- \tag{9}$$

$$H_2CO_3 + OH^- \leftrightarrow HCO_3^- + H_2O \tag{10}$$

$$HCO_3^- + OH^- \leftrightarrow CO_3^{2-} + H_2O \tag{11}$$

$$Ca^{2+} + CO_3^{2-} \leftrightarrow CaCO_3 \tag{12}$$

The mass conservation of urea can be estimated using the Michaelis–Menten equation due to its reliable performance [30, 44, 45]:

$$\frac{\partial nC_{urea}}{\partial t} = \nabla(nD\nabla C_{urea}) - \nabla(vC_{urea}) - R_u \tag{13}$$

$$R_u = n \cdot C_b \cdot UA \cdot \frac{C_{urea}}{K_m + C_{urea}} \tag{14}$$

where C_{urea} is urea concentration (mol/L), K_m is half saturation constant (mol/L), C_b is the total bacteria (OD), $C_b = C_{bs} + \rho_b \cdot C_{batt}$, UA is the specific urease activity of bacteria (mmol/L/min/OD). It is noted that the precipitation kinetics of CaCO$_3$ depend on the activities of carbonate and calcium ions, and the solubility product of CaCO$_3$ [46]. Correspondingly, a saturation-dependent model has been proposed to describe the CaCO$_3$ precipitation process [47]. However, this equation is relatively complex, requiring the estimation of many parameters such as activity coefficients and specific surface area [48]. Additionally, the solubility constants for different CaCO$_3$ morphologies vary, with values 10$^{-6.62}$, 10$^{-7.91}$, 10$^{-8.34}$, and 10$^{-8.48}$ for ikaite, vaterite, aragonite, and calcite, respectively [49]. For ease of calculation, a "Single reaction model" was proposed for estimating the precipitation kinetics in MICP/EICP [50]:

$$CO(NH_2)_2 + 2H_2O + Ca^{2+} \rightarrow 2NH_4^+ + CaCO_3 \tag{15}$$
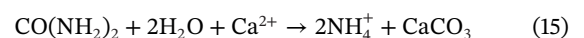
Assuming that the precipitation rate is equal to the urea hydrolysis rate, that is, $R_p = R_u$ (mmol/L/min), in the presence of sufficient calcium, the mass conservation equations for Ca^{2+} and $CaCO_3$ are:

$$\frac{\partial nC_{Ca}}{\partial t} = \nabla \left(nD \nabla C_{Ca} \right) - \nabla \left(v C_{Ca} \right) - R_p \tag{16}$$

$$\frac{\partial C_{CaCO_3}}{\partial t} = M_{CaCO_3} R_p / \rho_b \tag{17}$$

where C_{Ca} is the concentration of calcium (mol/L), C_{CaCO_3} is the $CaCO_3$ content precipitated in soils (g/g), and M_{CaCO_3} is the molar mass of $CaCO_3$ (100 g/mol).

As noted by previous researchers, the precipitation of $CaCO_3$ simultaneously affects both fluid flow [51] and soil permeability [52] due to changes in pore structure [53]. At the macroscale, variations in porosity and permeability are of greater interest than detailed changes in pore structure. Therefore, we focused solely on changes in porosity and the resulting variations in permeability. The reduction in porosity can be described by:

$$\frac{\partial n}{\partial t} = -\frac{\rho_b}{\rho_{CaCO_3}} \frac{\partial C_{CaCO_3}}{\partial t} \tag{18}$$

where ρ_{CaCO_3} is the dry density of $CaCO_3$, (g/cm^3).

The relationship between changes in porosity and permeability was thoroughly reviewed by Hommel et al. [15]. The reduction in permeability is primarily attributed to changes in the pore throat when $CaCO_3$ precipitation occurs. In this study, the Kozeny-Carman model is used to describe the porosity-induced permeability change:

$$\frac{K_{kc}}{K_0} = \frac{n^3(1-n_0)^2}{n_0^3(1-n)^2} \tag{19}$$

$$K_0 = \frac{d^2}{180} \cdot \frac{n_0^3}{(1-n_0)^2} \tag{20}$$

where K_{kc} is the permeability calculated using the Kozeny–Carman relationship (m^2); K_0 is the initial permeability (m^2).

Additionally, the precipitation of $CaCO_3$ can encapsulate bacteria leading to a decrease in the reaction rate. As the encapsulated bacteria are linked to both the total bacteria count and the quantity of precipitated $CaCO_3$, by introducing an encapsulation coefficient, k_{en} ((OD·m^3)/kg), we can obtain $\Delta C_{b\_en} = k_{en} \cdot C_b \cdot \Delta C_{CaCO_3}$. The changes in encapsulated bacteria over time are intricately connected to the rate of $CaCO_3$ precipitation, that is, $\Delta C_{b\_en}/\Delta t = k_{en} \cdot C_b \cdot \Delta C_{CaCO_3}/\Delta t$. Subsequently, by considering an infinitesimal time interval, we can obtain the encapsulation rate, R_{en}, of bacteria:

$$R_{en} = k_{en} \cdot (C_{bs} + \rho_b C_{batt}) \cdot \frac{\partial C_{CaCO_3}}{\partial t} \tag{21}$$

The above model was solved using COMSOL Multiphysics software based on the Finite element method (FEM). Fluid flow was described using *Darcy's Flow*, while the transport of bacteria and chemicals was described using two separate *Transport of Diluted Species in Porous Media* modules. The adsorption and desorption of bacteria, along with chemical reactions, were defined using reaction elements under the *Transport of Diluted Species in Porous Media* module. Variations in $CaCO_3$ contents and porosity were computed using two additional ordinary differential equations (ODEs). The permeability variation was defined by a local function.

3 | Model Verification

3.1 | Homogeneous Soil Condition

The accuracy of the model was verified using the experimental test conducted by Whiffin et al. [54]. In their work, a vertically positioned sand column with a diameter of 66 mm and a length of 5 m was used. The sand column was prepared with Itterbeck sand, having a dry density of 1.65 g/cm^3 and an initial hydraulic conductivity of 2×10^{-5} m/s. Solutions were injected from top to bottom at a hydraulic head of 5 m, with an approximate flow rate of 0.35 L/h. The injection strategy was as follows: The sand column was flushed with tap water for 30.7 h. Bacterial suspension with an OD_{600} of 1.583 and urease activity of 0.23 mS/min was injected for 18.1 h. A 0.05 mol/L $CaCl_2$ solution was injected for 17.1 h. A cementation solution containing 1.1 mol/L urea and $CaCl_2$ was injected for 24.9 h. A no-flow period of 102 h was allowed for the reaction to occur. The sand column was rinsed by injecting tap water for 23.7 h. The distribution of $CaCO_3$ content along the length of the sand column was used to calibrate the model. Table 2 lists the values of the parameters used in the model.

Figure 2 depicts the established 2D-axisymmetric model and compares the numerical and experimental results. The distribution of adsorbed bacteria is also presented in Figure 2b, which indicates that the bacteria adsorbed in the sand first increased and then decreased along the flow direction, which is similar to the findings reported by Martinez et al. [25]. The results demonstrate that the constructed model can reasonably capture the experimental observations.

3.2 | Layered Soil Condition

The natural ground typically consists of strata with varying soil properties due to seasonal variations in flood, river, lake, and sea conditions [55, 56]. These differences in soil properties across strata result in variations in permeability and bacterial attachment, leading to differences in cementation levels. In this study, we primarily investigate the influence of soil stratum heterogeneity on the MICP process. Additionally, we consider the effects of injection strategy and reaction rate which significantly impact the Péclet number (Pe) and Damköhler number (Da), that is, parameters that describe the interaction between chemical reactions, diffusion, and transport [57, 58]. The main parameters and their values are listed in Table 3. The staged injection strategy is employed for solution injection. Within a single injection cycle, the bacterial solution is initially injected at a specified hydraulic head for one hour, followed by the injection of the cementation solution for another hour. Subsequently, a static reaction period of 10 h ensues. To attain a higher level of cementation, the aforementioned injection cycle is reiterated, a process that can

TABLE 2 | Values of the parameters used in the model for simulating the results of Whiffin et al. [54].

| Parameters	Definitions	Values	Parameters	Definitions	Values
$n_0(1)$	Porosity	0.378	k_{det} (1/s)	Detachment coefficient	2×10^{-5}
ρ_b (kg/m^3)	Dry density of sand	1650	k_{en} ((OD·m^3)/kg)	Encapsulation coefficient	1×10^{-5}
K_0 (m^2)	Permeability	2.04×10^{-12}	UA (mol/L/s/OD)	Urease activity	0.011
v_{in} (m/s)	Injection velocity	2.84×10^{-5}	$C_{0,urea}$ (mol/L)	Initial urea concentration	1.1
$C_{0,bs}$(OD)	Bacterial density	1.583	K_m (mol/L)	Half saturation constant	0.055
D (m^2/s)	Dispersion/diffusion	1×10^{-9}	M_{CaCO_3} (g/mol)	Molar mass of CaCO$_3$	100
k_{att} (1/s)	Attachment coefficient	2.5×10^{-4}	ρ_{CaCO_3} (kg/m^3)	Density of CaCO$_3$	2710
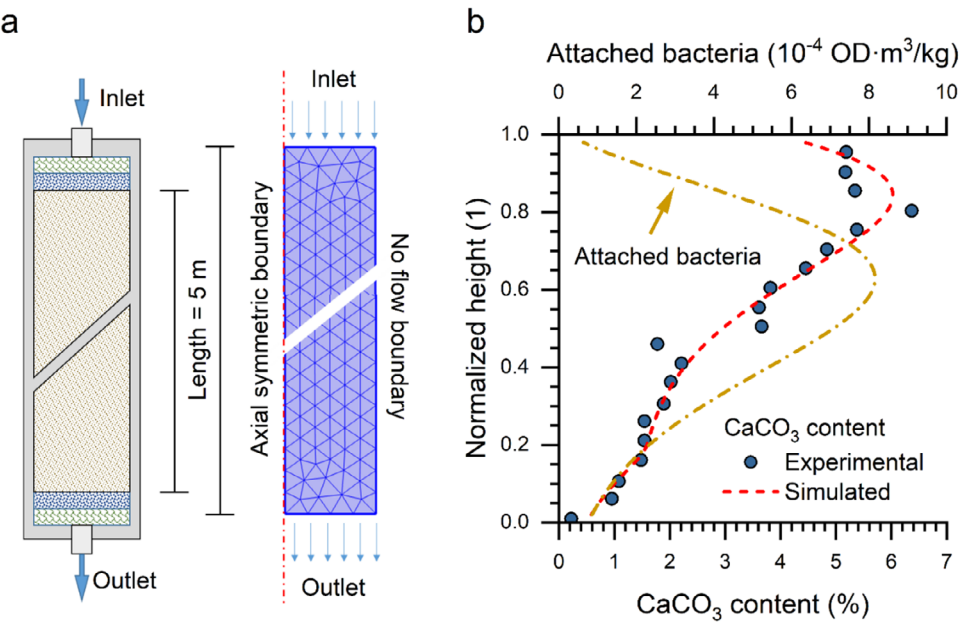
FIGURE 2 | (a) Details about the model [54] and (b) the comparison of experimental and simulated results.

TABLE 3 | Main parameters and their values.

Main factors		Values				
Soil heterogeneity	Geometry[a] (Ht, %)	0	25	50	75	100
	Particle size (d_{50}, mm)	Coarse 0.71		Medium 0.36		Fine 0.15
	Porosity (n, −)	0.35		0.4		0.45
Injection	Hydraulic head (HD, m)	5		10		20
Reaction	Urease activity (UA, mmol/L/min)	1		10		20

[a]The geometry is the height ratio of the top soil layer. At 0% and 100%, the soil is homogeneous. At 25%, the height of the top soil layer corresponds to 1/4 of the total model height, as is the case for other percentages as well.
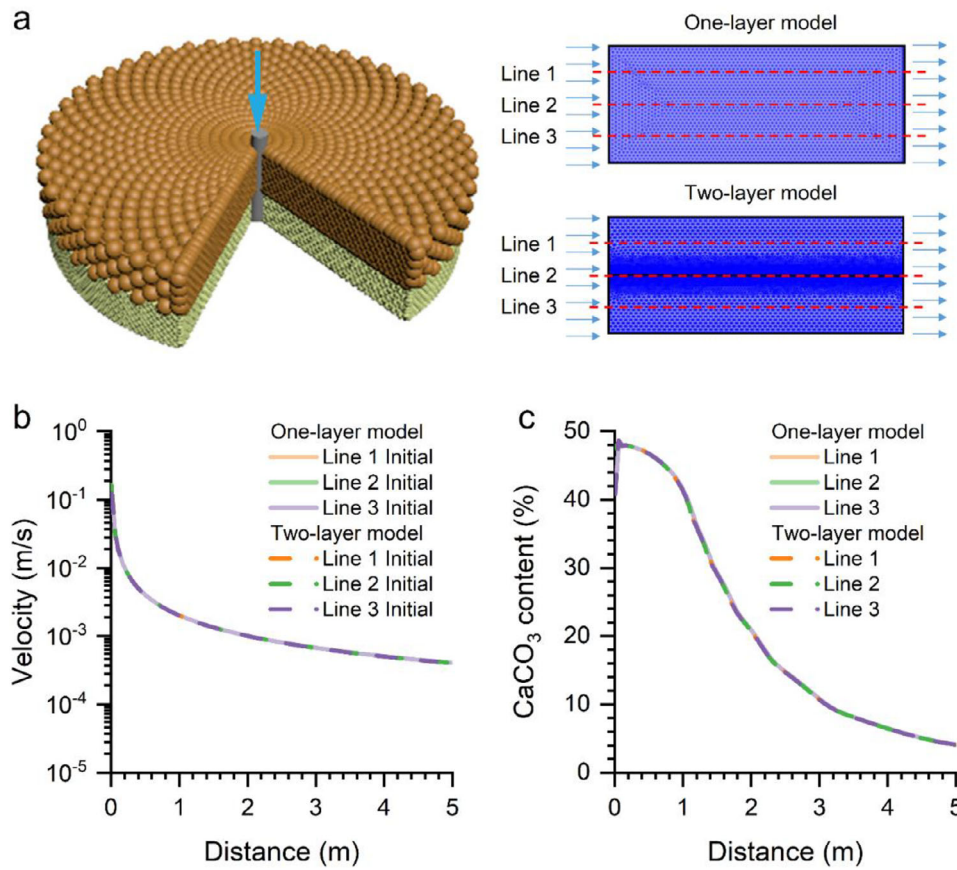
FIGURE 3 | (a) Schematic view of the two-layer model and (b) comparison of the results calculated by the one-layer model and two-layer model.

be facilitated by defining three piecewise functions for injection, bacterial density, and chemical concentration.

To verify the validity of the newly constructed two-layer model, as illustrated in Figure 3a, the results are compared with those of the one-layer model (No. HO1). It can be observed that the distribution of velocity and $CaCO_3$ content along the three specific lines are comparable between the two models. Therefore, the two-layer model is used in the subsequent analysis. The details of the parameters used for the stabilization of homogeneous and heterogeneous soils are listed in Table 4. Given the significance of injection rate and flow velocity in comprehending the grouting processes, we have included their respective values. It is noteworthy that the solutions are influenced by the hydraulic head, and the permeability of soils fluctuates after each cycle. Hence, we have provided the values for each treatment cycle in Table 5.

4 | Results and Discussion

4.1 | Effect of Injection Parameters and Soil Properties

In this section, we first explore the influence of injection parameters and soil properties on MICP grouting in homogeneous soils, which will serve as a comparison basis for layered heterogeneous soils. The distribution of attached bacteria and $CaCO_3$ after each treatment is displayed in Figures 4 and 5. It is evident that

the amount of attached bacteria, precipitated $CaCO_3$, and their distributions are affected by factors such as soil particle size, porosity, injection hydraulic head, and the urease activity of bacteria. For example, both the attached bacteria and precipitated $CaCO_3$ content are typically higher at the upstream part under most conditions. However, for the case of HO3, the attached bacteria and the distribution of $CaCO_3$ are relatively uniform.

Next, the $CaCO_3$ increment after each treatment cycle was also calculated, as shown in Figure 6. Based on the $CaCO_3$ increment, two important parameters were derived: the coefficient of variation (COV) [45, 59] and the average $CaCO_3$ increment (ΔC_{Ca}), to better understand the uniformity and efficiency of the precipitation after each treatment cycle:

$$\sigma = \frac{1}{n} \sum_{i=1}^{n} \sqrt{\left(\Delta C_{Ca,i} - \Delta C_{Ca}\right)^2} \qquad (22)$$

$$COV = \sigma / \Delta C_{Ca} \qquad (23)$$

Moreover, the precipitation efficiency and $CaCO_3$ distribution depend on the interaction between advection, diffusion, and reaction during MICP. Therefore, revised dimensionless parameters Péclet number (Pe) and Damköhler number (Da) are introduced:

$$Pe = \frac{\bar{u} \cdot d}{D} \qquad (24)$$

$$Da = \frac{UA \cdot (\rho_b \cdot C_{batt})/(K_m + C_{0urea})}{v/(\phi \cdot L)} \qquad (25)$$

TABLE 4 | Details for the test design.

Model	No.	Aim	Ht (m)	d_{50} (mm)	n (−)	UA (U)	HD (m)
Homogeneous	HO1	Control	0	0.36	0.4	10	10
	HO2	Particle size	0	0.15	0.4	10	10
	HO3		0	0.71	0.4	10	10
	HO4	Porosity	0	0.36	0.35	10	10
	HO5		0	0.36	0.45	10	10
	HO6	Hydraulic head	0	0.36	0.4	10	5
	HO7		0	0.36	0.4	10	20
	HO8	Urease activity	0	0.36	0.4	1	10
	HO9		0	0.36	0.4	20	10
Heterogeneous	HT0	Control	50	0.71	0.4	10	10
				0.15	0.4		
	HT1		50	0.71	0.45	10	10
				0.15	0.35		
	HT2	Location	50	0.15	0.35	10	10
				0.71	0.45		
	HT3	Geometry	25	0.71	0.45	10	10
				0.15	0.35		
	HT4		75	0.71	0.45	10	10
				0.15	0.35		
	HT5	Particle size	50	0.71	0.4	10	10
				0.36	0.4		
	HT6		50	0.36	0.4	10	10
				0.15	0.4		
	HT7	Porosity	50	0.36	0.45	10	10
				0.36	0.4		
	HT8		50	0.36	0.4	10	10
				0.36	0.35		
	HT9		50	0.36	0.45	10	10
				0.36	0.35		
	HT10	Hydraulic head	50	0.71	0.45	10	5
				0.15	0.35		
	HT11		50	0.71	0.45	10	20
				0.15	0.35		
	HT12	Urease activity	50	0.71	0.45	1	10
				0.15	0.35		
	HT13		50	0.71	0.45	20	10
				0.15	0.35		

Note: Ht, d_{50}, n, UA, and HD are the height of the top layer, median particle size, porosity, urease activity, and hydraulic head, respectively.

TABLE 5 | Injection rate and average flow velocity for homogeneous soils.

No.	Injection rate (m³/s)				Average flow velocity (m/s)			
	Cycle 1	**Cycle 2**	**Cycle 3**	**Cycle 4**	**Cycle 1**	**Cycle 2**	**Cycle 3**	**Cycle 4**
HO1	$1.4e^{-2}$	$1.2e^{-2}$	$7.8e^{-3}$	$4.8e^{-3}$	$8.0e^{-4}$	$6.6e^{-4}$	$4.4e^{-4}$	$2.6e^{-4}$
HO2	$2.4e^{-3}$	$1.8e^{-3}$	$9.1e^{-4}$	$3.8e^{-4}$	$1.4e^{-4}$	$1.0e^{-4}$	$5.1e^{-5}$	$2.1e^{-5}$
HO3	$5.5e^{-2}$	$4.9e^{-2}$	$3.9e^{-2}$	$2.9e^{-2}$	$3.1e^{-3}$	$2.8e^{-3}$	$2.2e^{-3}$	$1.6e^{-3}$
HO4	$8.1e^{-3}$	$6.8e^{-3}$	$4.8e^{-3}$	$3.1e^{-3}$	$4.6e^{-4}$	$3.9e^{-4}$	$2.7e^{-4}$	$1.7e^{-4}$
HO5	$2.4e^{-2}$	$1.9e^{-2}$	$1.2e^{-2}$	$7.2e^{-3}$	$1.4e^{-3}$	$1.1e^{-3}$	$6.9e^{-4}$	$3.9e^{-4}$
HO6	$7.1e^{-3}$	$5.8e^{-3}$	$4.0e^{-3}$	$2.5e^{-3}$	$3.9e^{-4}$	$3.3e^{-4}$	$2.3e^{-4}$	$1.4e^{-4}$
HO7	$2.8e^{-2}$	$2.3e^{-2}$	$1.5e^{-2}$	$9.2e^{-3}$	$1.6e^{-3}$	$1.3e^{-3}$	$8.7e^{-4}$	$5.1e^{-4}$
HO8	$1.4e^{-2}$	$1.4e^{-2}$	$1.3e^{-2}$	$1.2e^{-2}$	$8.1e^{-4}$	$7.8e^{-4}$	$7.4e^{-4}$	$6.8e^{-4}$
HO9	$1.3e^{-2}$	$5.9e^{-3}$	$1.3e^{-3}$	$2.4e^{-4}$	$7.7e^{-4}$	$3.4e^{-4}$	$7.0e^{-5}$	$1.2e^{-5}$

Pe is determined by the ratio of advection to diffusion, and Da is determined by the ratio of reaction rate to advection. The dependence of COV and ΔC_{Ca} on Pe and Da is illustrated in Figure 7. It can be observed that COV typically decreases with increasing Pe value and decreasing Da value, indicating that the CaCO$_3$ distribution is more uniform under advection-controlled grouting conditions. However, under very high velocity conditions (e.g., HO3, coarse sand) or very low bacteria (e.g., HO8) conditions, a contradicting phenomenon occurs: COV slightly increases with increasing Pe and decreasing Da. The slight increment in COV under these two conditions can be attributed to that more precipitates form downstream after each treatment cycle (Figure 6). However, this vairations did not greatly affect the uniformity of CaCO$_3$ distribution, as shown in Figure 5, the distribution of CaCO$_3$ is still relatively uniform compared to other conditions. Therefore, we can conclude that the uniformity of MICP grouting initially improves with increasing Pe and decreasing Da, but then slightly decreases with further increases in Pe and decreases in Da.

The ΔC_{Ca} after each treatment cycle first increases and then decreases with increasing Pe and Da. The peak of ΔC_{Ca} occurs at Pe values of 100–1000 and Da values of 0.1–1, which generally corresponds to the conditions for the most uniform CaCO$_3$ distribution. The results indicate that a more uniform CaCO$_3$ distribution leads to higher precipitate efficiency in homogeneous soils, and thus appropriate Pe and Da values should be selected during MICP grouting considering the cost-performance of treatment.

4.2 | Effect of Soil Heterogeneity

In this part, we discuss the CaCO$_3$ distribution and the flow field in two-layer heterogeneous models composed of soils of different particle sizes and porosities. The flow field during the 4th injection of cementation solution and the distribution of CaCO$_3$ after the 4th cycle of treatment are presented in Figures 8 and 9. In homogeneous models, solutions flow horizontally through the soils, while in the heterogeneous models, part of the solution passes through the interface between the two soil layers, transporting solutions of higher concentration to the downstream

section of the less permeable soil. As a result, more CaCO$_3$ precipitates near the interface compared to the areas far from the interface, forming a wedge-shaped increment of CaCO$_3$ in the less permeable soil. However, outside this wedge-shaped region, the CaCO$_3$ distribution is comparable to that observed in corresponding homogeneous soils.

By comparing Figures 8 and 9, it becomes clear that particle size has a more significant effect than porosity, as the wedge-shaped area is noticeably larger in the case of varying particle sizes. We attribute this to the combined influence of soil properties, bacteria adsorption, and the flow field. When the soil particle size increases from 0.15 to 0.75 mm, permeability increases by 22.4 times, and the attachment coefficient decreases by approximately 3.8 times. In contrast, when the porosity increases from 0.35 to 0.45, permeability increases by 2.31 times, and the attachment coefficient decreases by approximately 1.18 times. Additionally, only a small amount of solution flows through the interface at the midsection of the model when the porosity changes from 0.35 to 0.45. However, a significant amount of solution flows through the interface from the upstream to the outlet when particle sizes change from 0.15 to 0.75 mm.

To investigate the longitudinal and vertical distribution of CaCO$_3$ in layered soils, and to compare the results with those in homogeneous soils, we selected two horizontal lines located at the middle of each layer, and three vertical lines located at distances of 0.1, 1, and 3 m from the central line. Interestingly, the CaCO$_3$ distribution along the horizontal lines is comparable to that in the corresponding homogeneous soil. The results suggest that the influence of soil heterogeneity on the distribution of CaCO$_3$ is typically limited to a distance of less than 0.5 m.

The vertical distribution of CaCO$_3$ shows that, from the high-permeable to the low-permeable soil layers, CaCO$_3$ content remains constant in high-permeable soils but increases sharply at the soil layer interface. After that, CaCO$_3$ content quickly decreases to the same level as that in the corresponding low-permeable homogeneous soil and remains constant. Notably, the influence of soil heterogeneity is most significant in the midstream section. Specifically, as shown in Figure 8a, the CaCO$_3$ content slightly increases at the interface and then
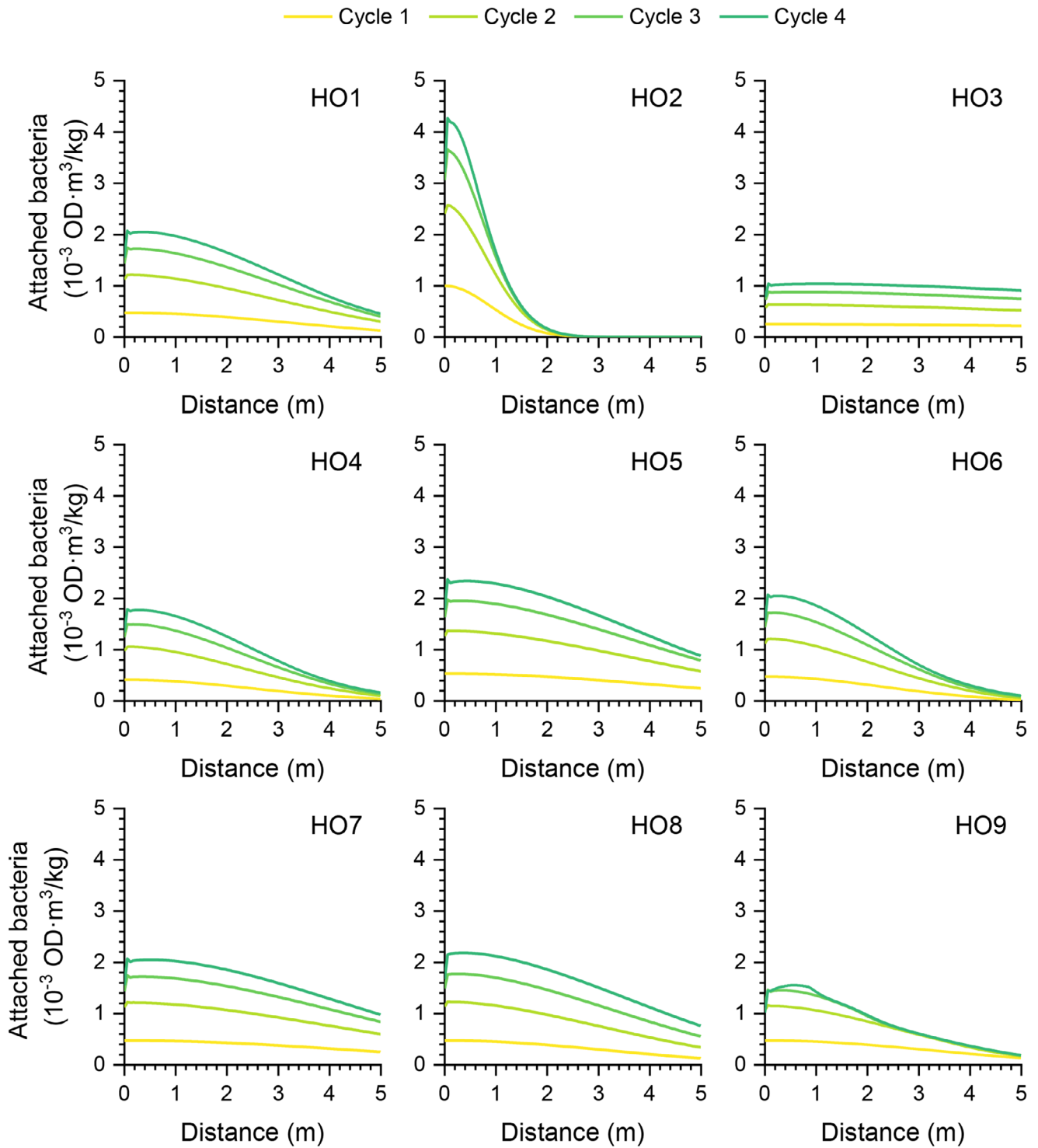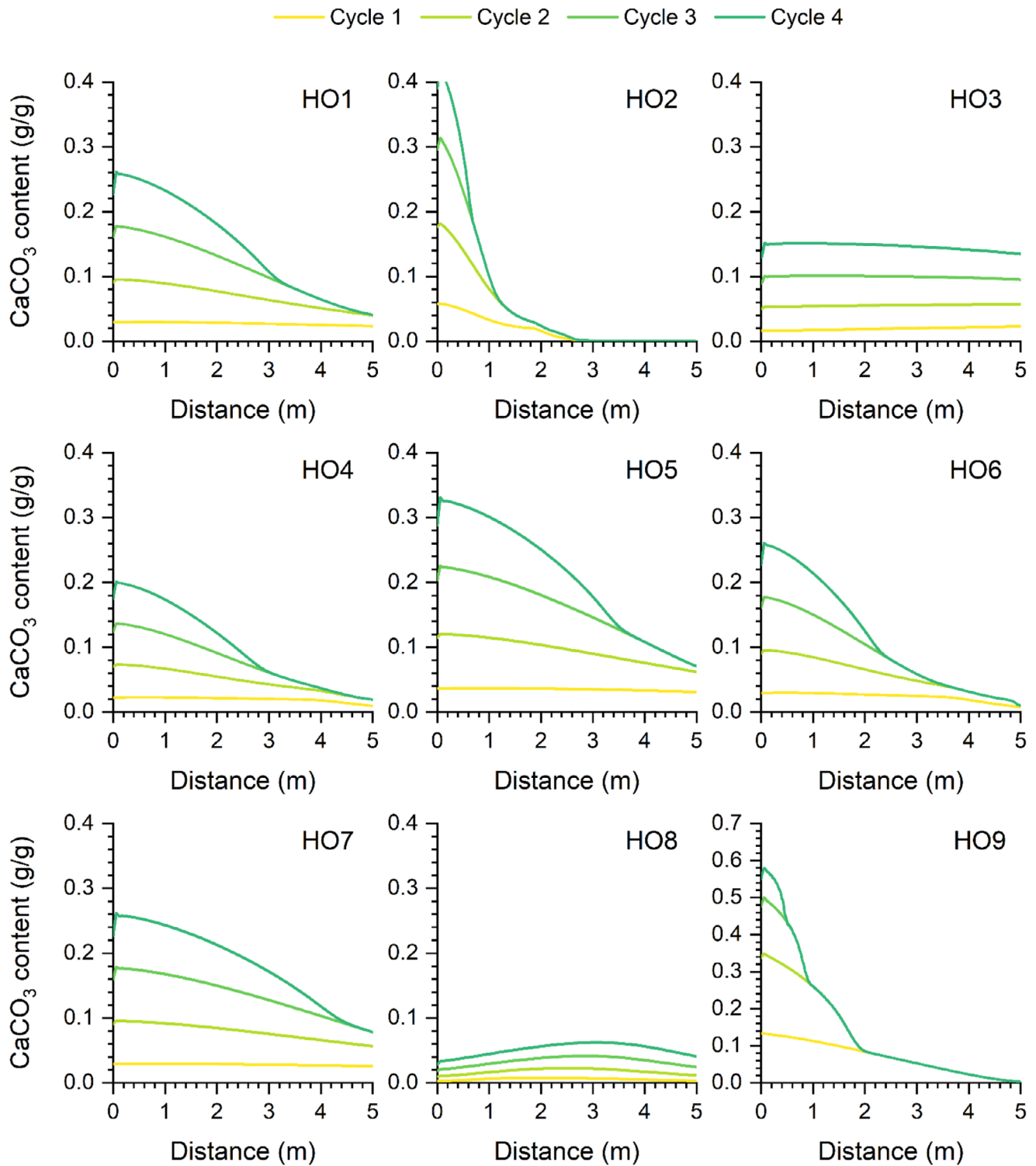
FIGURE 4 | Distribution of attached bacteria along radial direction in homogeneous soils after the injection of cementation solutions.

sharply decreases along the L1 line, while the $CaCO_3$ content significantly increases and decreases at a slower rate along the L2 line. The variations in $CaCO_3$ content along the L3 line fall between those of L1 and L2. It appears that the greater the soil heterogeneity, that is, the difference in particle size and porosity between soil layers, the higher the peak of $CaCO_3$ content at the soil layer interface and the larger the zone of $CaCO_3$ increment in the low-permeable soil layer. However, outside this increment zone, the $CaCO_3$ content is compara-

ble to that in the corresponding homogeneous low-permeable soils.

## 4.3 | Effect of the Location and Geometry of the Soil Layer

In the previous section, the two-layer soil models consisted of a high-permeable top layer and a low-permeable bottom layer. In

FIGURE 5 | Distribution of CaCO₃ content along radial direction in homogeneous soils after each treatment cycle.

this section, we present the results for the opposite arrangement, where the high-permeable layer is at the bottom and the low-permeable layer is at the top. The distribution of attached bacteria after the injection of bacterial solution and the distribution of CaCO₃ after each treatment cycle along selected vertical and horizontal lines are presented in Figure 10. Along the horizontal direction, the distribution of attached bacteria and CaCO₃ in the top layer of HT1 is comparable to that in the bottom layer of HT2, and vice versa. Along the vertical direction, the attached bacteria and CaCO₃ content are symmetric along the interface between the two soil layers. These results indicate that the position of the high- and low-permeable soil layers does not obviously influence the distribution of attached bacteria and CaCO₃ content in each layer of the two-layer soil model.
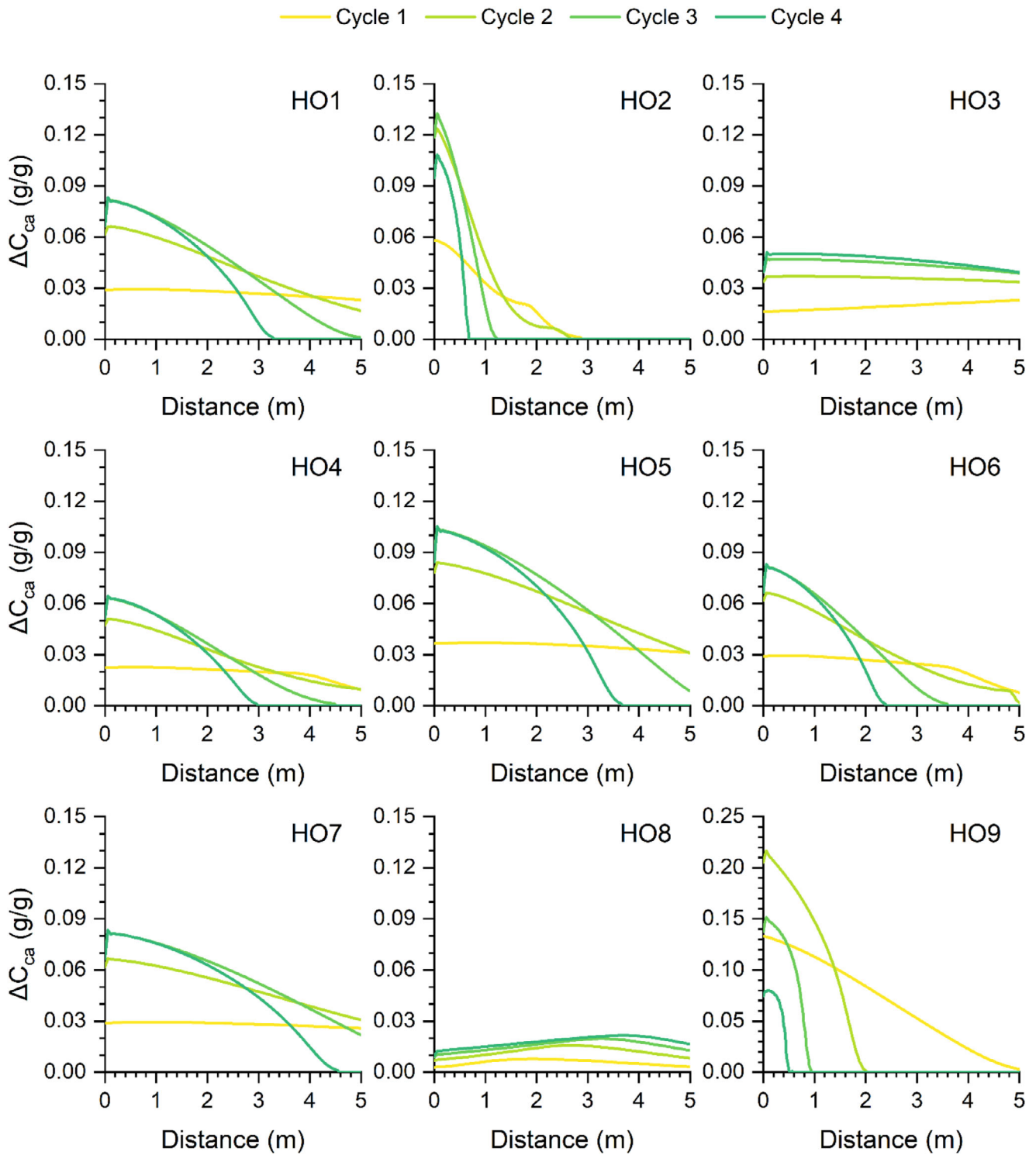
FIGURE 6 | Distribution of the CaCO$_3$ increment in homogeneous soils after each treatment cycle.

Additionally, we investigated the effect of soil layer thickness on the distribution of attached bacteria and CaCO$_3$. Along the horizontal central line of the top high-permeable layer, the distribution of attached bacteria and CaCO$_3$ is similar across the three cases (HT1, HT3, and HT4). However, in the bottom low-permeable soil, the distribution is notably affected by the thickness of the layers. For example, as shown in Figure 11c,d, at a distance of 1 m, the CaCO$_3$ content at the central point is 5.2% in the bottom layer of HT3, while it is 9.2% in the bottom layer

of HT4 after the 4th cycle of treatment. Furthermore, the CaCO$_3$ content drops to 0 at a distance of 2.4 m in the bottom layer of HT3, compared to 2.8 m in the bottom layer of HT4.

The vertical distribution of the attached bacteria and CaCO$_3$ shows a similar trend across the three cases, as mentioned above, with the maximum CaCO$_3$ content being the same for all three cases. However, the zone influenced by soil heterogeneity depends on the thickness of the soil layer. For example, in a
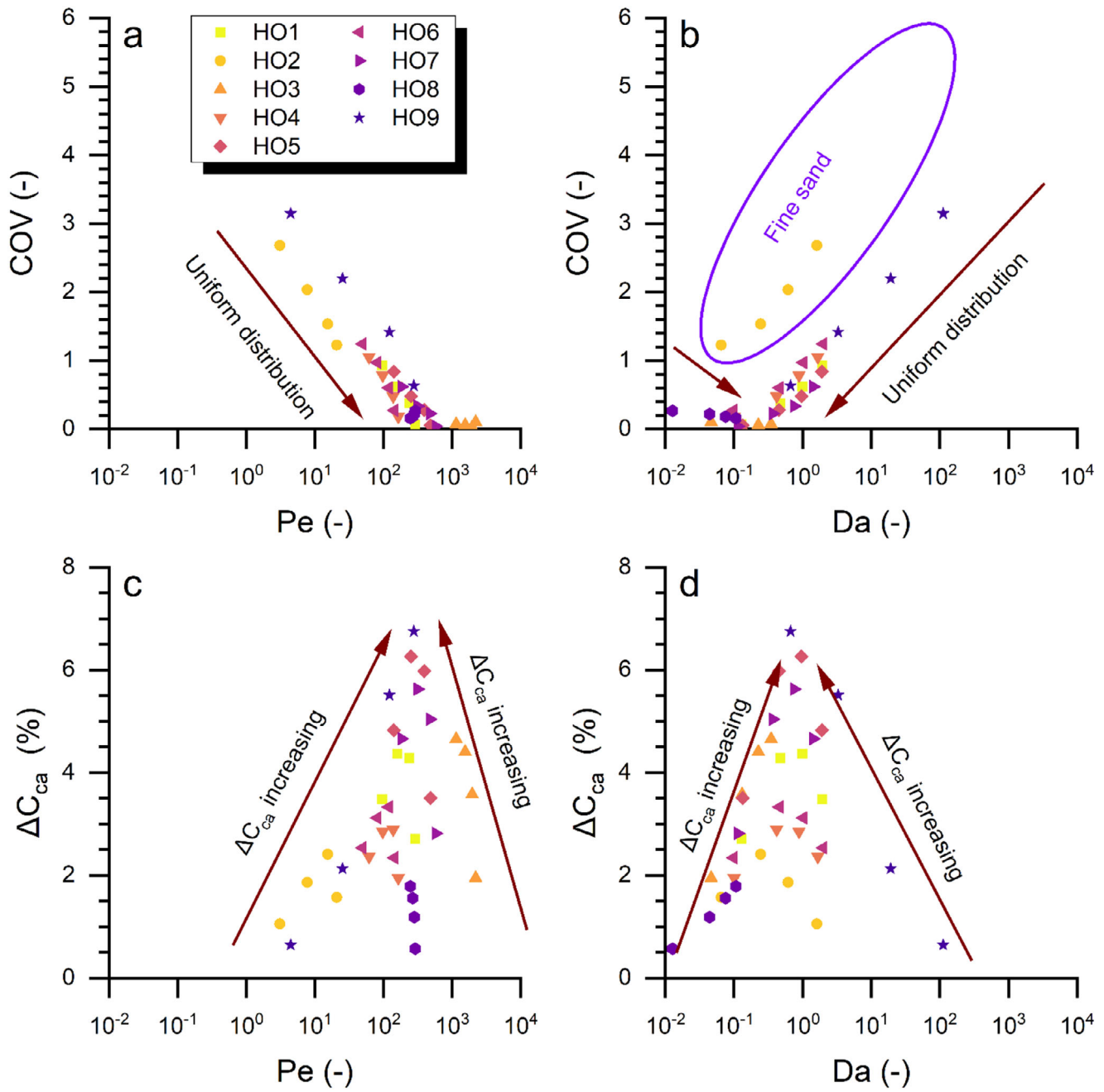
FIGURE 7 | Dependence of COV on (a) *Pe* and (b) *Da*, and ΔC_{Ca} on (c) *Pe* and (d) *Da* in homogeneous soils.

thicker low-permeable layer, the $CaCO_3$ content decreases more slowly than in a thinner layer, particularly in the mid- and downstream sections.

4.4 | Discussion for Layered Soils

In this section, we discuss the effects of differences in soil properties between two soil layers, hydraulic head, and urease activity on the distribution of $CaCO_3$ in layered soils. Since the distribution of $CaCO_3$ in the high-permeable layer of the models is comparable to that in homogeneous high-permeable soils, soil layering does not obviously affect the distribution of $CaCO_3$ in the high-permeable soil layer. Therefore, the focus of this

discussion is on the distribution of $CaCO_3$ in the low-permeable layer, specifically the horizontal distribution of $CaCO_3$ at different depths, the area of the ZOI, and the average $CaCO_3$ increment (ΔC_{ca}) in the low-permeable soil of two-layer models.

First, ten horizontal lines were selected from the soil layer interface to the bottom of the low-permeable layer at 0.1 m intervals, and the distribution of $CaCO_3$ along these lines was collected, as shown in Figure 12. The influence of the soil layering on the distribution of $CaCO_3$ in the low-permeable layer is not obvious under the conditions of HT7, HT8, and HT9, which were set to explore the effect of porosity. Specifically, the impact of the soil layering is limited to less than 0.1 m in the vertical direction. These results suggest that the difference in porosity between the
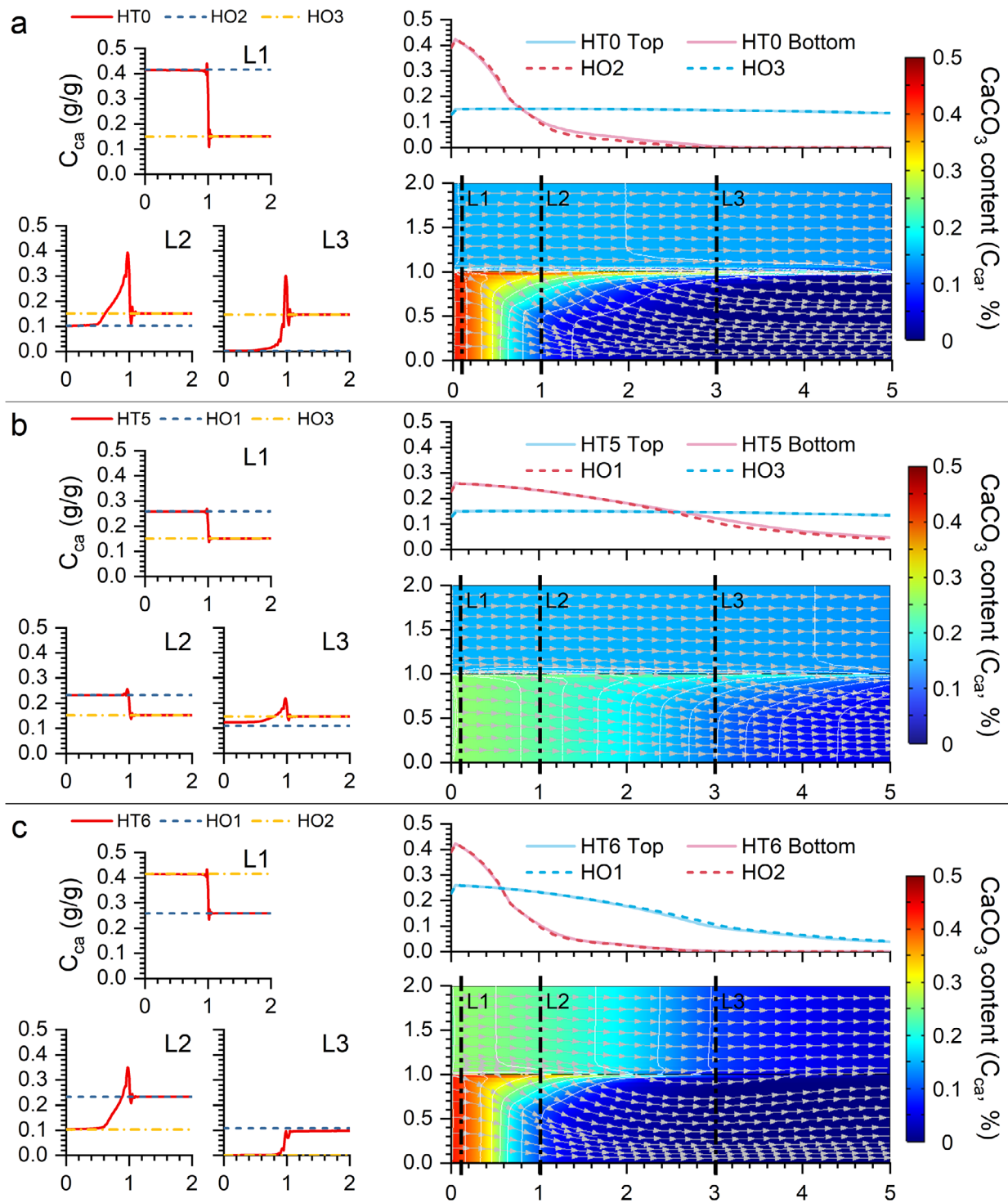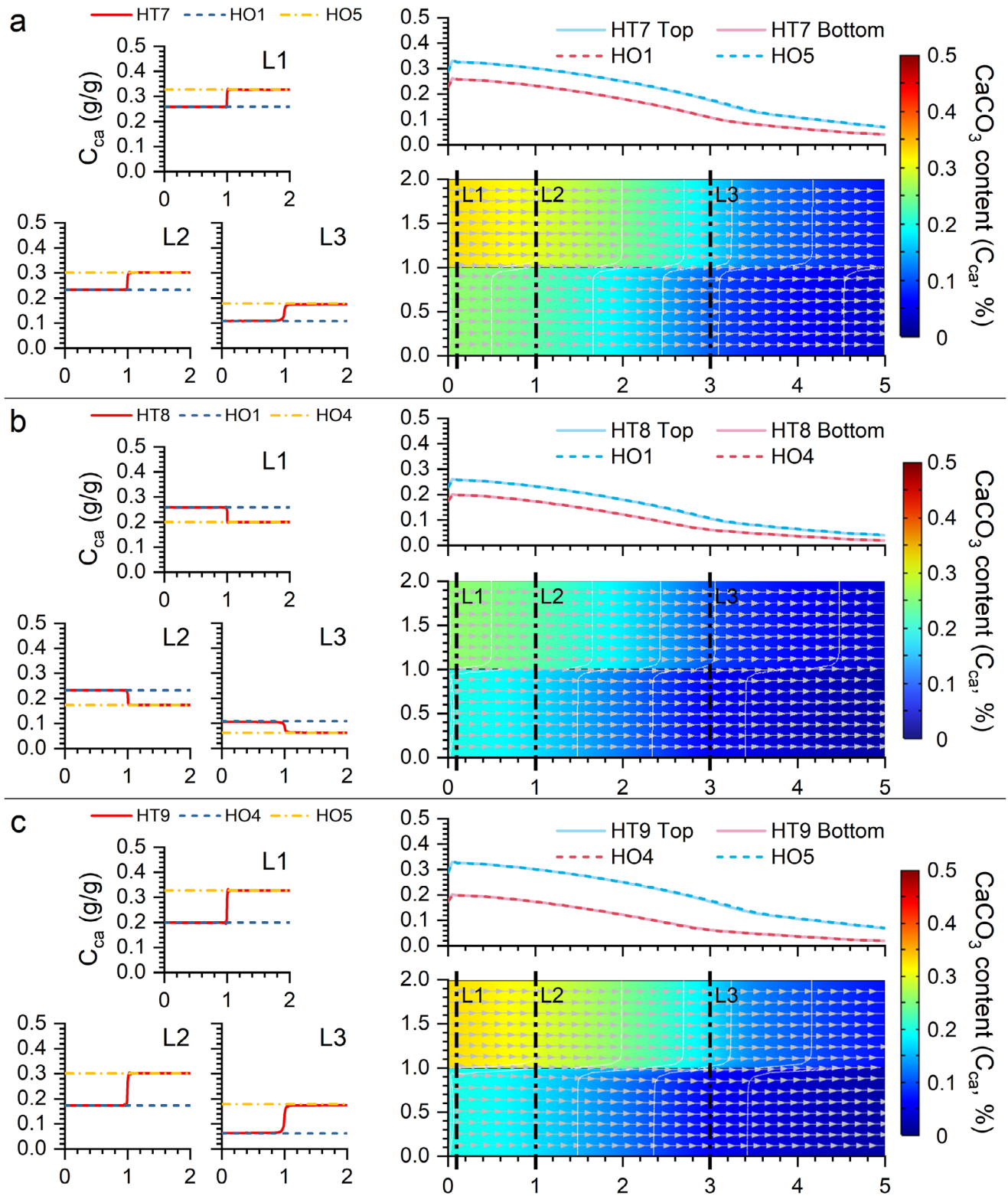
FIGURE 8 | Influence of the difference on the particle sizes of the two soil layers on the flow field and CaCO$_3$ distribution in layered heterogeneous soils.

two soil layers does not substantially affect the distribution of CaCO$_3$ in layered soils.

However, the difference in particle size between soil layers appears to have a much more pronounced effect on the distribution of CaCO$_3$ in the low-permeable layers, with CaCO$_3$ precipitation still being enhanced at depths of 0.5 ∼ 0.6 m. Additionally, in the results of HT12, it can be observed that at very

low urease activity, the impact of soil layering on the distribution of CaCO$_3$ is diminished, as CaCO$_3$ precipitation is only enhanced at depths of less than 0.2 m.

To calculate the area of ZOI, we extract characteristic points where CaCO$_3$ precipitation in the low-permeable soil layer is enhanced. For example, in the case of HT0, the CaCO$_3$ content deviates from the rest of the soil at a distance of approximately

FIGURE 9 | Influence of the difference on the porosities of the two soil layers on the flow field and CaCO₃ distribution in layered heterogeneous soils.

0.4 m from the −0.1 m line and converges again at about 4.2 m. These characteristic points are gathered, and the area enveloped by these points is calculated, as presented in Figure 13a. It should be noted that the areas are calculated based on the selected lines at 0.1 m intervals, leading to a potential error of less than 0.5 m². As shown in Figure 13b, the areas of ZOI for HT7, HT8, and HT9 are almost zero, indicating minimal enhancement of CaCO₃ precipitation. The areas of ZOI for HT1, HT5, and HT6 are relatively large and comparable, covering about 28% of the total area of the low-permeable layer. Additionally, injection parameters also
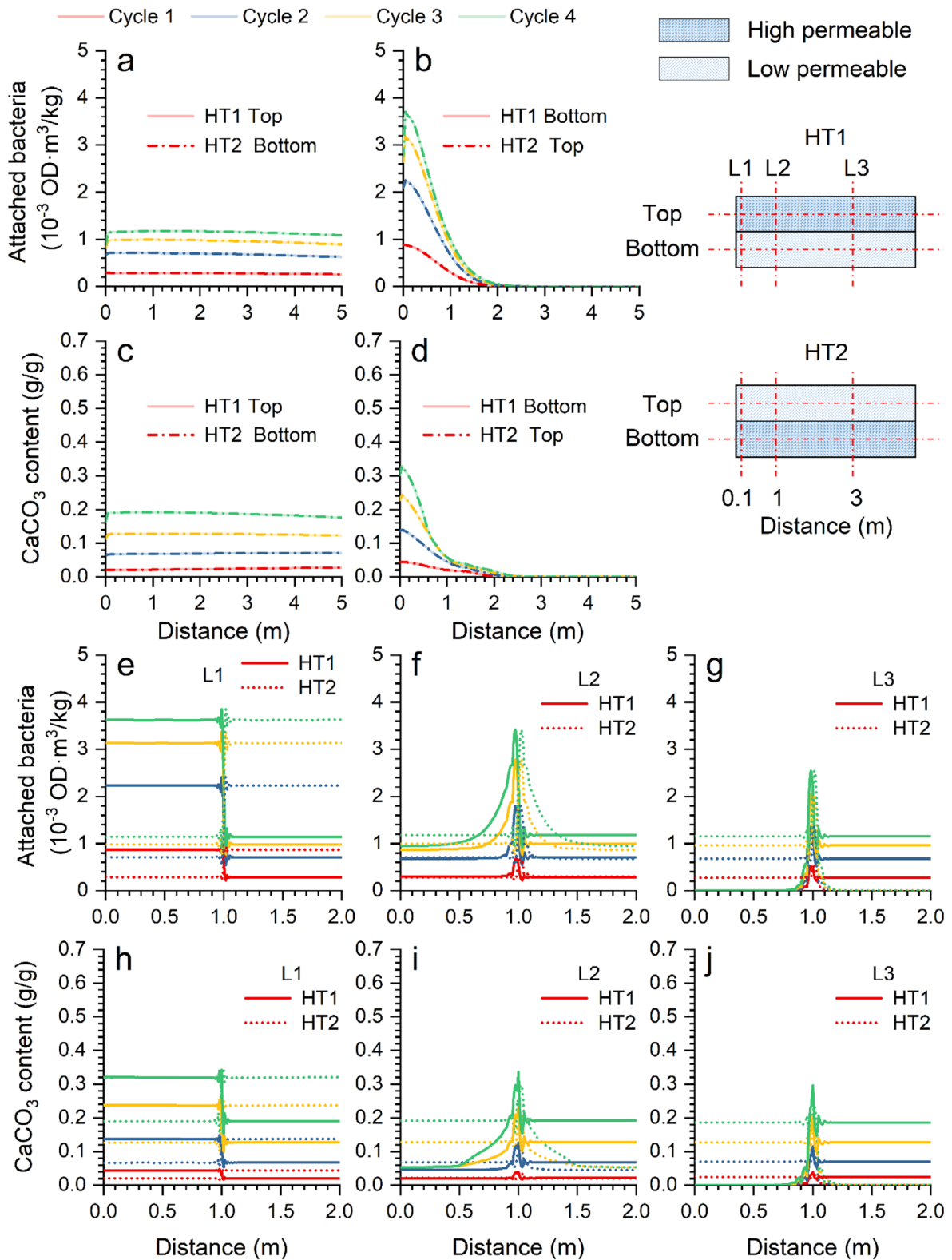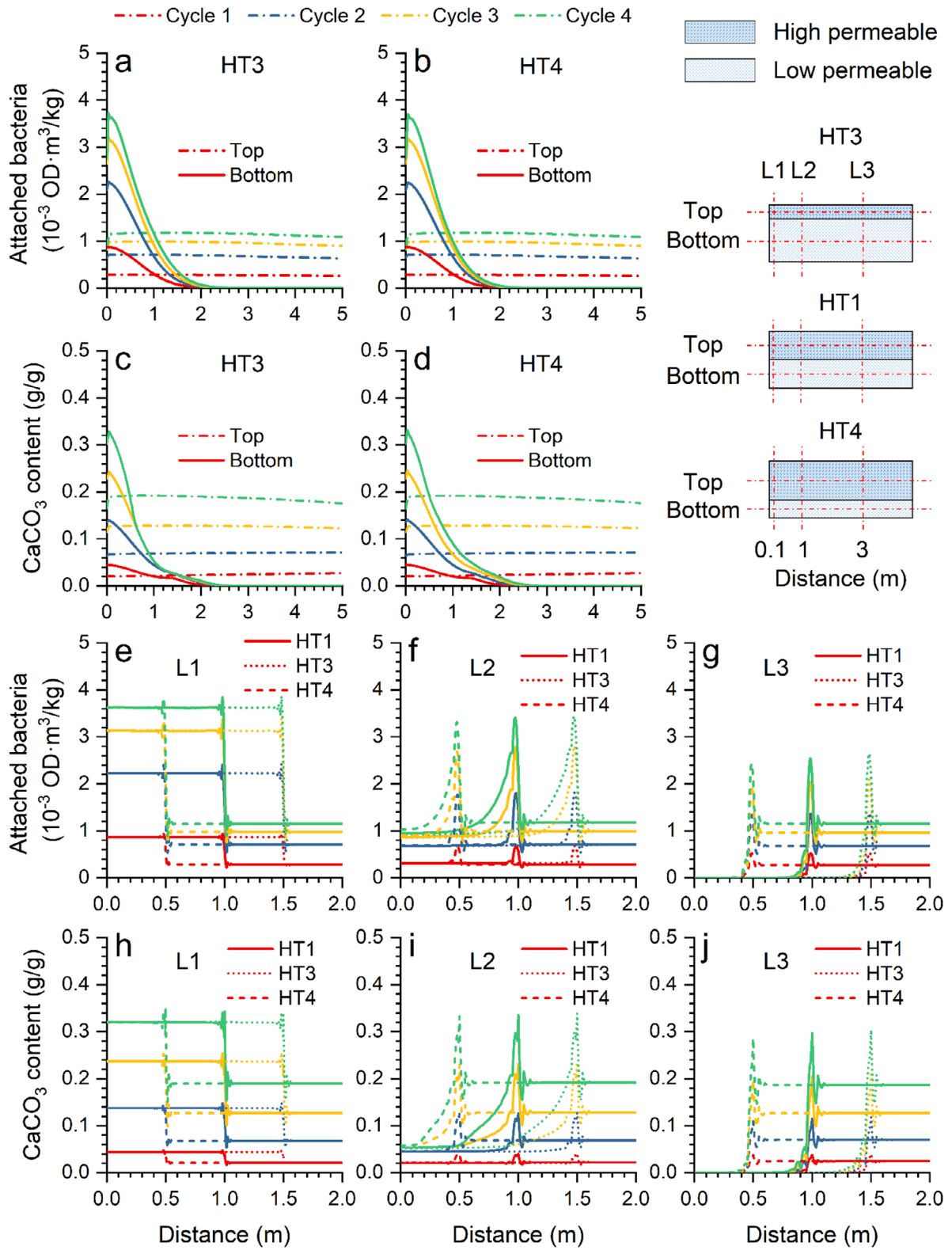
FIGURE 10 | The influence of the location of the soil layers on the attached bacteria and CaCO₃ content.

affect the area of ZOI. Specifically, the area of ZOI for HT10 (20%) is smaller than that of HT1 (40%), while the area of ZOI for HT11 (46%) is larger than that of HT1 (40%). This indicates that higher injection velocities lead to larger areas of ZOI. However, the areas of ZOI for HT12 and HT13 are both smaller than that of HT1, suggesting that very low or very high urease activity results in a smaller ZOI.

Furthermore, we can investigate ΔC_{ca} in the low-permeable soil layer caused by soil layering, based on the results from Figure 12.

FIGURE 11 | The influence of heights of soil layers on the attached bacteria and CaCO$_3$ content.

Specifically, the average CaCO$_3$ content ($\overline{C_{ca}}$) in the cross-section of the layered soils can be integrated from lines H1 to H10

$$\overline{C_{ca}} = \frac{1}{S} \int_{-1}^{0} \int_{0.01}^{5} C_{ca} \, dl \, dh \approx \frac{1}{10} \sum \frac{\Delta h}{S_{sub}} \int_{0.01}^{5} C_{ca} \, dl \quad (26)$$

where S is the area of the bulk low-permeable soil layer, l and h are the length and height of each soil layer, and Δh and S_{sub} are the height and area of each divided layer. The average CaCO$_3$ content in the corresponding homogeneous soil $\overline{C_{caho}}$ can be obtained by integrating line H10, as the influence of the soil layering is typically less than approximately 0.6 m, and the CaCO$_3$ content
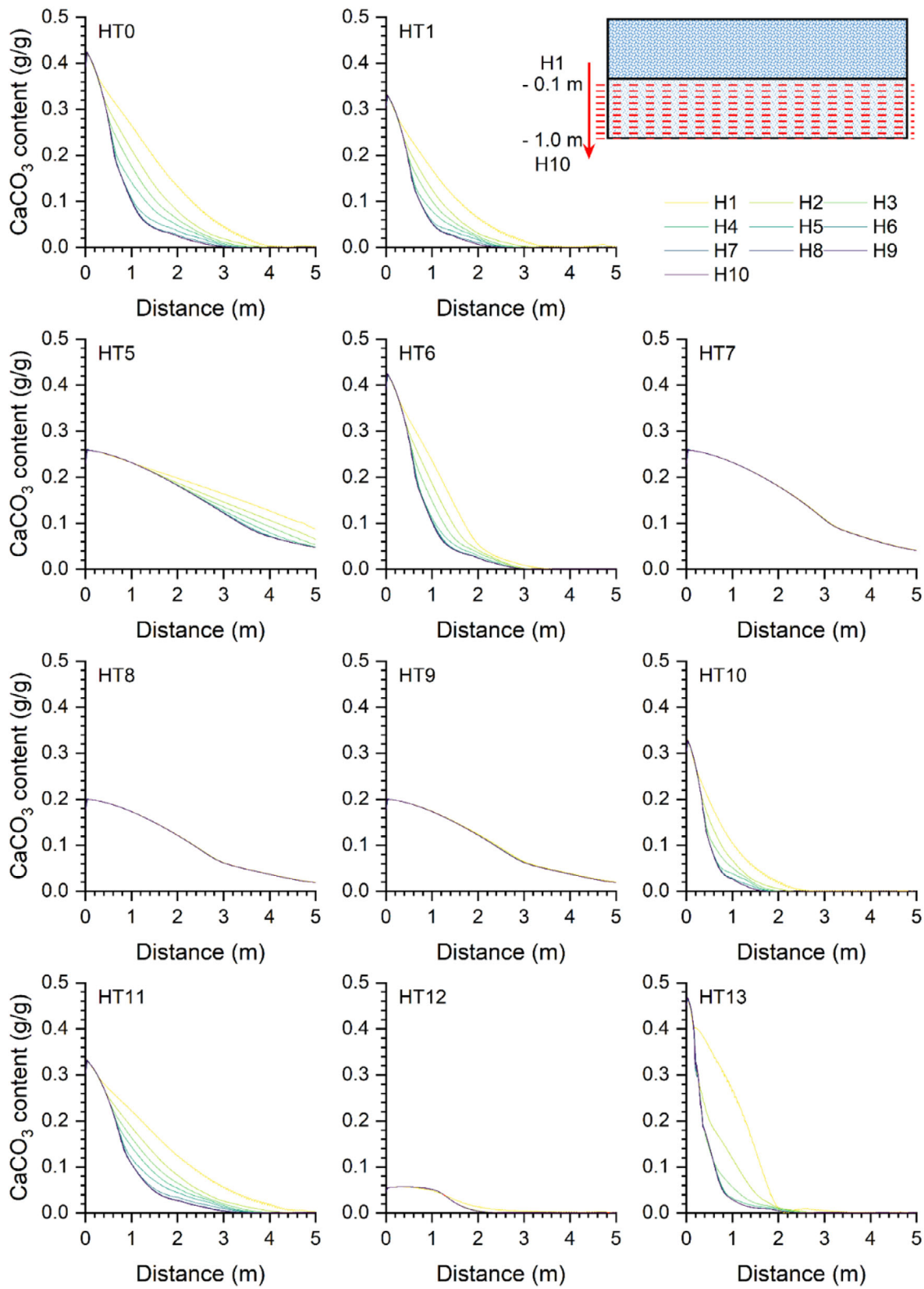
FIGURE 12 | The distribution of $CaCO_3$ after the 4th treatment along radial direction at different heights in the low-permeable soil layers.

in the remaining part is comparable to that in the corresponding homogeneous soils:

$$\overline{C_{caho}} = \frac{1}{S} \int_{-1}^{0} \int_{0.01}^{5} C_{ca} dl dh = \frac{H}{S} \int_{0.01}^{5} C_{ca} dl \qquad (27)$$

where H is the height of the low-permeable soil. Therefore, ΔC_{ca} can be calculated as:

$$\Delta C_{ca} = \frac{\overline{C_{ca}} - \overline{C_{caho}}}{\overline{C_{caho}}} \qquad (28)$$
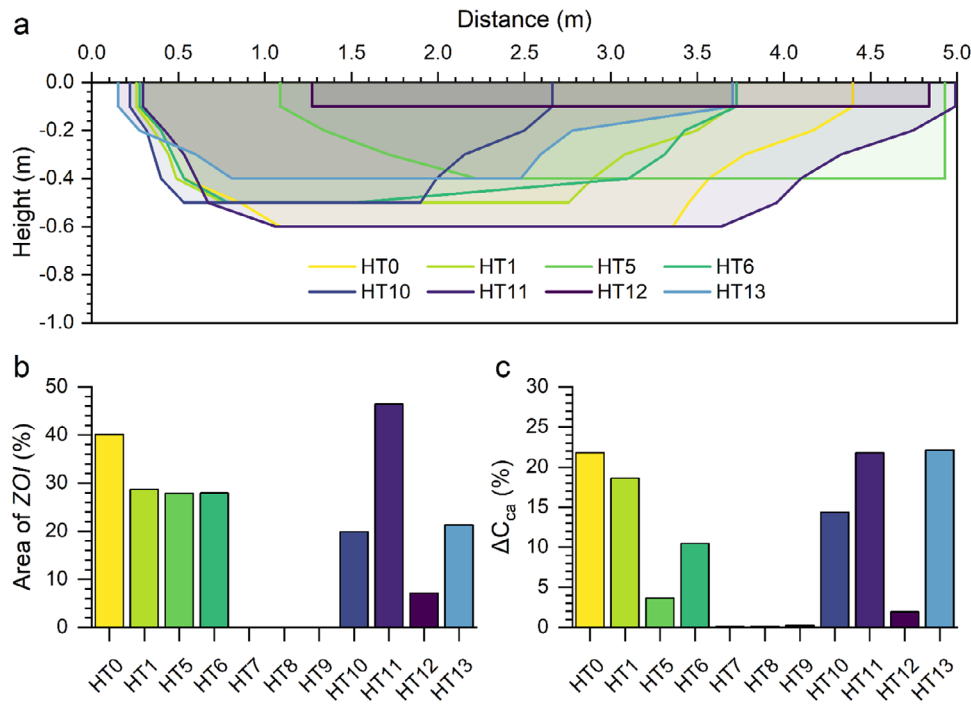
FIGURE 13 | (a) Schematic view of the zone of influence (ZOI) in the low-permeable soil layers, (b) the area of ZOI, and (c) ΔC_{ca} in the low-permeable soil layer of the two-layer models.

As shown in Figure 13b, there is almost no CaCO$_3$ increment in HT7, HT8, and HT9. The values of ΔC_{ca} in the low-permeable soils of HT0, HT1, HT11, and HT13 are relatively large, while those of HT5 and HT12 are relatively small. It can be observed that the CaCO$_3$ increment is generally consistent with the area of *ZOI* when the injection parameters are similar. However, ΔC_{ca} can be further influenced by the urease activity of bacteria. For example, although the area of *ZOI* in HT11 is significantly larger than that in HT13, the values of ΔC_{ca} in HT11 and HT13 are comparable. Additionally, particle size can influence ΔC_{ca} because it affects the adsorption of bacteria. For example, the areas of *ZOI* in HT5 and HT1 are comparable, the ΔC_{ca} in HT5 is obviously lower than that in HT1.

4.5 | Limitations and Perspectives

It should also be noted that in this work, the volume of the injected solutions was controlled by the injection duration and hydraulic head, rather than the pore volume of soils. Sufficient solutions were injected into the soils, with more than one pore volume of solution being injected into the low-permeable layer, ensuring its effective stabilization. However, in engineering practice, it is important to control material costs. As a result, the volume of injected solutions is often controlled by the pore volume, or a circulating grouting method is used, as seen in previous studies. In future work, it will be necessary to further study the influence of injection strategies on the performance and uniformity of MICP stabilization.

Furthermore, the pivotal discovery in our current study—namely, the creation of a wedge-shaped CaCO$_3$ increment region in low-permeable soil during the grouting of layered heterogeneous soils—serves not only to deepen our comprehension of the impact of soil heterogeneity on MICP grouting but also to optimize soil stabilization through this phenomenon. To illustrate, for expediting the stabilization of fine sand, we can introduce two high-permeable soil layers to facilitate the transportation of bacteria and chemicals, thereby enhancing the efficiency and uniformity of cementation—a task often challenging in low-permeable soils like in case HO2. Future research endeavors will entail numerical and experimental validations to substantiate this concept.

5 | Conclusions

In this work, a reactive transport model was developed to simulate MICP grouting in both homogeneous and layered heterogeneous soils, capturing the hydrological, biological, and chemical processes involved. The effects of soil properties, injection hydraulic head, and urease activity on the distribution of bacteria and CaCO$_3$ content in homogeneous soils were first examined, followed by an analysis of how differences in these parameters between two soil layers influence the distribution of CaCO$_3$ in layered soils. The main conclusions drawn from this study are as follows:

1. In homogeneous soils, the efficiency and uniformity of MICP grouting are affected by soil particle size, soil porosity, injection hydraulic head, and urease activity. The uniformity and efficiency of MICP grouting are primarily governed by the interaction between advection, diffusion, and reaction, which are characterized by the Peclet number (*Pe*) and Damköhler number (*Da*).

2. Generally, $CaCO_3$ content decreases with increasing distance from the injection point, while its uniformity improves with increasing Pe and decreasing Da. However, in cases with very high velocity and low urease activity, more precipitates tend to form in the downstream region, that is, when Pe increases further and Da decreases a slight reduction in the uniformity of MICP grouting will be ovserved. The average $CaCO_3$ increment after each treatment cycle initially increases and then decreases with increasing Pe and Da. Notably, the peak values of the average $CaCO_3$ increment typically occur at similar Pe and Da values to those associated with the most uniform $CaCO_3$ distribution, indicating that a more uniform distribution of $CaCO_3$ leads to higher precipitate efficiency in homogeneous soils.

3. In layered heterogeneous soils, a key observation is that part of the solutions flows through the interface between the two soil layers, transporting solutions of higher concentration to the downstream region of the less permeable soils. This leads to a greater amount of $CaCO_3$ precipitating near the interface, creating a wedge-shaped distribution in the less permeable layer. Beyond this wedge-shaped region, the $CaCO_3$ distribution is comparable to that in the corresponding homogeneous soils.

4. The difference in the particle size between the two soil layers has a more significant influence on $CaCO_3$ distribution than porosity, as the area of the wedge-shaped region (ZOI) is considerably larger in the case of varying particle sizes. Furthermore, the influence of soil layering is also affected by the injection hydraulic head and urease activity. Specifically, a higher injection hydraulic head results in a larger ZOI. However, very low or very high urease activity leads to a smaller ZOI.

5. The average $CaCO_3$ increment (ΔC_{ca}) in the low-permeable soil layer was also quantitatively analyzed. ΔC_{ca} is generally consistent with the area of ZOI when the injection parameters are similar, that is, a larger ZOI corresponds to a higher ΔC_{ca}. However, ΔC_{ca} can also be influenced by bacterial activity in the low-permeable layer. Generally, when urease activity is lower or fewer bacteria are adsorbed, ΔC_{ca} in the low-permeable soils is relatively small.

The results of this work highlight that the distribution of $CaCO_3$ and the average precipitate content in layered heterogeneous soils can be divided into three regions: the high-permeable region, the low-permeable region adjacent to the interface, and the low-permeable region far from the interface. In the high-permeable region and the low-permeable region far from the interface, the $CaCO_3$ distribution and average precipitate content are comparable to those in corresponding homogeneous soils. However, the $CaCO_3$ content increases in the low-permeable region adjacent to the interface. Therefore, when applying MICP to stabilize layered heterogeneous soils, it is crucial to determine the area of the zone of influence and the $CaCO_3$ increment in this zone.

Conflicts of Interest

The authors declare no conflicts of interest.

Data Availability Statement

All data that support the findings of this study are available from the corresponding author upon reasonable request.

References

1. X. Yu and H. Rong, "Seawater Based MICP Cements Two/One-Phase Cemented Sand Blocks," *Applied Ocean Research* 118 (2022): 102972, https://doi.org/10.1016/j.apor.2021.102972.

2. X. Yu and Z. Zhang, "Calcium Carbide Sludge Activated Fly Ash Mixture for Offshore Construction and Its Crack Repair Using Seawater-Mixed Bioslurry Cement," *Journal of Cleaner Production* 395 (2023): 136456, https://doi.org/10.1016/j.jclepro.2023.136456.

3. C. Qian, X. Yu, T. Zheng, and Y. Chen, "Review on Bacteria Fixing CO_2 and Bio-Mineralization to Enhance the Performance of Construction Materials," *Journal of CO2 Utilization* 55 (2022): 101849, https://doi.org/10.1016/j.jcou.2021.101849.

4. D.-L. Wang, C.-S. Tang, X.-H. Pan, et al., "Construction and Demolition Waste Stabilization Through a Bio-Carbonation of Reactive Magnesia Cement for Underwater Engineering," *Construction and Building Materials* 335 (2022): 127458, https://doi.org/10.1016/j.conbuildmat.2022.127458.

5. D.-L. Wang, C.-S. Tang, X.-H. Pan, et al., "A Novel Bio-Carbonation Method of Reactive Magnesia With Urea Pre-Hydrolysis for Geomaterial Stabilisation," *Géotechnique* 74, no. 13 (2023): 1634–1648, https://doi.org/10.1680/jgeot.22.00301.

6. Y. Xiao, X. He, A. W. Studelein, J. Chu, T. M. Evans, and L. A. van Paassen, "Crystal Growth of MICP Through Microfluidic Chip Tests," *Journal of Geotechnical and Geoenvironmental Engineering* 148, no. 5 (2022): 06022002, https://doi.org/10.1061/(asce)gt.1943-5606.0002756.

7. G. Ma, X. He, Y. Xiao, et al., "Spatiotemporal Evolution of Biomineralization in Heterogeneous Pore Structure," *Canadian Geotechnical Journal* 61, no. 3 (2024): 447–468, https://doi.org/10.1139/cgj-2022-0496.

8. L. Cheng, M. A. Shahin, and J. Chu, "Soil Bio-Cementation Using a New One-Phase Low-pH Injection Method," *Acta Geotechnica* 14, no. 3 (2019): 615–626, https://doi.org/10.1007/s11440-018-0738-2.

9. M. P. Harkes, L. A. Van Paassen, J. L. Booster, V. S. Whiffin, and M. C. M. Van Loosdrecht, "Fixation and Distribution of Bacterial Activity in Sand to Induce Carbonate Precipitation for Ground Reinforcement," *Ecological Engineering* 36, no. 2 (2010): 112–117, https://doi.org/10.1016/j.ecoleng.2009.01.004.

10. H. A. Keykha, B. B. K. Huat, and A. Asadi, "Electrokinetic Stabilization of Soft Soil Using Carbonate-Producing Bacteria," *Geotechnical and Geological Engineering* 32, no. 4 (2014): 739–747, https://doi.org/10.1007/s10706-014-9753-8.

11. G. Sang, R. J. Lunn, G. El Mountassir, and J. M. Minto, "Transport and Fate of Ureolytic *Sporosarcina pasteurii* in Saturated Sand Columns: Experiments and Modelling," *Transport in Porous Media* 149, no. 2 (2023): 599–624, https://doi.org/10.1007/s11242-023-01973-x.

12. D. J. Tobler, M. O. Cuthbert, and V. R. Phoenix, "Transport of *Sporosarcina pasteurii* in Sandstone and Its Significance for Subsurface Engineering Technologies," *Applied Geochemistry* 42 (2014): 38–44, https://doi.org/10.1016/j.apgeochem.2014.01.004.

13. Y. Wang, Y. Wang, K. Soga, J. T. DeJong, and A. J. Kabla, "Microscale Investigations of Temperature-Dependent Microbially Induced Carbonate Precipitation (MICP) in the Temperature Range 4–50°C," *Acta*

Geotechnica 18, no. 4 (2022): 2239–2261, https://doi.org/10.1007/s11440-022-01664-9.

14. C. Zhao, Y. Xiao, J. Chu, et al., "Microfluidic Experiments of Biological CaCO₃ Precipitation in Transverse Mixing Reactive Environments," *Acta Geotechnica* 18, no. 10 (2023): 5299–5318, https://doi.org/10.1007/s11440-023-01938-w.

15. J. Hommel, E. Coltman, and H. Class, "Porosity–Permeability Relations for Evolving Pore Space: A Review With a Focus on (bio-)Geochemically Altered Porous media," *Transport in Porous Media* 124, no. 2 (2018): 589–629, https://doi.org/10.1007/s11242-018-1086-2.

16. J. M. Minto, E. MacLachlan, G. El Mountassir, and R. J. Lunn, "Rock Fracture Grouting With Microbially Induced Carbonate Precipitation," *Water Resources Research* 52, no. 11 (2016): 8827–8844, https://doi.org/10.1002/2016wr018884.

17. D. H. Kim, N. Mahabadi, J. Jang, and L. A. van Paassen, "Assessing the Kinetics and Pore-Scale Characteristics of Biological Calcium Carbonate Precipitation in Porous media Using a Microfluidic Chip Experiment," *Water Resources Research* 56, no. 2 (2020): e2019WR025420, https://doi.org/10.1029/2019wr025420.

18. M. G. Gomez, B. C. Martinez, J. T. DeJong, et al., "Field-Scale Bio-Cementation Tests to Improve Sands," *Proceedings of the Institution of Civil Engineers—Ground Improvement* 168, no. 3 (2015): 206–216, https://doi.org/10.1680/grim.13.00052.

19. B. C. Martinez and J. T. Dejong, "Bio-Mediated Soil Improvement: Load Transfer Mechanisms at the Micro- and Macro-Scales," *Geotechnical Special Publication* no. 188 (2009): 242–251, https://doi.org/10.1061/41025(338)26.

20. Y. Xiao, X. He, W. Wu, et al., "Kinetic Biomineralization Through Microfluidic Chip Tests," *Acta Geotechnica* 16, no. 10 (2021): 3229–3237, https://doi.org/10.1007/s11440-021-01205-w.

21. D. Feng, X. Wang, U. Nackenhorst, X. Zhang, and P. Pan, "A Comparative Study of Using Two Numerical Strategies to Simulate the Biochemical Processes in Microbially Induced Calcite Precipitation," *Journal of Rock Mechanics and Geotechnical Engineering* 14, no. 2 (2022): 592–602, https://doi.org/10.1016/j.jrmge.2021.08.013.

22. X. Wang and U. Nackenhorst, "A Coupled Bio-Chemo-Hydraulic Model to Predict Porosity and Permeability Reduction During Microbially Induced Calcite Precipitation," *Advances in Water Resources* 140 (2020): 103563, https://doi.org/10.1016/j.advwatres.2020.103563.

23. Z. Faeli, B. M. Montoya, and M. A. Gabr, "Development of a Reactive Transport Model for Microbial Induced Calcium Carbonate Precipitation in Unsaturated Conditions," *Canadian Geotechnical Journal* 61, no. 4 (2023): 827–835, https://doi.org/10.1139/cgj-2022-0677.

24. S. Fauriel and L. Laloui, "A Bio-Chemo-Hydro-Mechanical Model for Microbially Induced Calcite Precipitation in Soils," *Computers and Geotechnics* 46 (2012): 104–120, https://doi.org/10.1016/j.compgeo.2012.05.017.

25. B. C. Martinez, J. T. DeJong, and T. R. Ginn, "Bio-Geochemical Reactive Transport Modeling of Microbial Induced Calcite Precipitation to Predict the Treatment of Sand in One-Dimensional Flow," *Computers and Geotechnics* 58 (2014): 1–13, https://doi.org/10.1016/j.compgeo.2014.01.013.

26. M. K. Nassar, D. Gurung, M. Bastani, et al., "Large-Scale Experiments in Microbially Induced Calcite Precipitation (MICP) Reactive Transport Model Development and Prediction," *Water Resources Research* 54 (2017): 180–500, https://doi.org/10.1002/2017WR021488.

27. O. Ramos and T.-H. Kwon, "Development of Bio-Grout Injection Strategy and Design Guide Using Reactive Transport Model for Field-Scale Soil Improvement Based on Microbially Induced Calcium Carbonate Precipitation (MICP)," *Geomechanics for Energy and the Environment* 36 (2023): 100509, https://doi.org/10.1016/j.gete.2023.100509.

28. M. O. Cuthbert, L. A. McMillan, S. Handley-Sidhu, M. S. Riley, D. J. Tobler, and V. R. Phoenix, "A Field and Modeling Study of Fractured Rock Permeability Reduction Using Microbially Induced Calcite Precipitation,"

Environmental Science & Technology 47, no. 23 (2013): 13637–13643, https://doi.org/10.1021/es402601g.

29. J. Wang, Y. Long, Y. Zhao, et al., "Numerical Simulation of Forming MICP Horizontal Seepage Reducing Body in Confined Aquifer for Deep Excavation," *Applied Sciences* 13, no. 1 (2023): 601, https://doi.org/10.3390/app13010601.

30. C. Zeng, Y. Veenis, C. A. Hall, et al., "Experimental and Numerical Analysis of a Field Trial Application of Microbially Induced Calcite Precipitation for Ground Stabilization," *Journal of Geotechnical and Geoenvironmental Engineering* 147, no. 7 (2021): 05021003, https://doi.org/10.1061/(asce)gt.1943-5606.0002545.

31. Y. Li, Z. Guo, L. Wang, and H. Yang, "A Coupled Bio-Chemo-Hydro-Wave Model and Multi-Stages for MICP in the Seabed," *Ocean Engineering* 280 (2023): 114667, https://doi.org/10.1016/j.oceaneng.2023.114667.

32. X. Y. Li, L. M. Zhang, H. Zhu, and J. H. Li, "Modeling Geologic Profiles Incorporating Interlayer and Intralayer Variabilities," *Journal of Geotechnical and Geoenvironmental Engineering* 144, no. 8 (2018): 04018047, https://doi.org/10.1061/(asce)gt.1943-5606.0001895.

33. Z. Qiu, J. Lu, A. Ebeido, et al., "Bridge in Narrow Waterway: Seismic Response and Liquefaction-Induced Deformations," *Journal of Geotechnical and Geoenvironmental Engineering* 148, no. 8 (2022): 04022064, https://doi.org/10.1061/(ASCE)GT.1943-5606.0002852.

34. A. Srivastava, G. L. S. Babu, and S. Haldar, "Influence of Spatial Variability of Permeability Property on Steady State Seepage Flow and Slope Stability Analysis," *Engineering Geology* 110, no. 3–4 (2010): 93–101, https://doi.org/10.1016/j.enggeo.2009.11.006.

35. D. Zhao, Y. Xia, C. Zhang, et al., "A New Method to Investigate the Size Effect and Anisotropy of Mechanical Properties of Columnar Jointed Rock Mass," *Rock Mechanics and Rock Engineering* 56, no. 4 (2022): 2829–2859, https://doi.org/10.1007/s00603-022-03200-3.

36. B. C. Martinez, J. T. Dejong, T. R. Ginn, et al., "Experimental Optimization of Microbial-Induced Carbonate Precipitation for Soil Improvement," *Journal of Geotechnical & Geoenvironmental Engineering* 139, no. 4 (2013): 587–598, https://doi.org/10.1061/ASCE)GT.1943-5606.0000787.

37. Z. Faeli, B. M. Montoya, and M. A. Gabr, "Various Bacterial Attachment Functions and Modeling of Biomass Distribution in MICP Implementations," *Journal of Geotechnical and Geoenvironmental Engineering* 149, no. 9 (2023): 04023064, https://doi.org/10.1061/jggefk.Gteng-10812.

38. L. Wang, L. van Paassen, V. Pham, N. Mahabadi, J. He, and Y. Gao, "A (simplified) Biogeochemical Numerical Model to Predict Saturation, Porosity and Permeability During Microbially Induced Desaturation and Precipitation," *Water Resources Research* 59, no. 1 (2023): e2022WR032907, https://doi.org/10.1029/2022wr032907.

39. W. K. van Wijngaarden, L. A. van Paassen, F. J. Vermolen, G. A. M. van Meurs, and C. Vuik, "A Reactive Transport Model for Biogrout Compared to Experimental Data," *Transport in Porous Media* 111, no. 3 (2015): 627–648, https://doi.org/10.1007/s11242-015-0615-5.

40. J. W. Foppen and J. F. Schijven, "Transport of *E. coli* in Columns of Geochemically Heterogeneous Sediment," *Water Research* 39, no. 13 (2005): 3082–3088, https://doi.org/10.1016/j.watres.2005.05.023.

41. H. H. M. Rijnaarts, W. Norde, E. J. Bouwer, J. Lyklema, and A. J. B. Zehnder, "Bacterial Deposition in Porous media Related to the Clean Bed Collision Efficiency and to Substratum Blocking by Attached Cells," *Environmental Science & Technology* 30, no. 10 (1996): 2869–2876, https://doi.org/10.1021/es960597b.

42. J. W. Foppen and J. F. Schijven, "Evaluation of Data From the Literature on the Transport and Survival of *Escherichia coli* and Thermotolerant Coliforms in Aquifers Under Saturated Conditions," *Water Research* 40, no. 3 (2006): 401–426, https://doi.org/10.1016/j.watres.2005.11.018.

43. S. A. Bradford, S. R. Yates, M. Bettahar, and J. Simunek, "Physical Factors Affecting the Transport and Fate of Colloids in Saturated Porous media," *Water Resources Research* 38, no. 12 (2002): 63–61–63–12, https://doi.org/10.1029/2002wr001340.

44. L. A. van Paassen, "*Biogrout, Ground Improvement by Mircobial Induced Carbonate Precipitation*" (PhD, Delft University of Technology, 2009).

45. Z. Faeli, B. M. Montoya, and M. A. Gabr, "Elucidating Factors Governing MICP Biogeochemical Processes at Macro-Scale: A Reactive Transport Model Development," *Computers and Geotechnics* 160 (2023): 105514, https://doi.org/10.1016/j.compgeo.2023.105514.

46. A. C. Mitchell and F. G. Ferris, "The Influence of *Bacillus pasteurii* on the Nucleation and Growth of Calcium Carbonate," *Geomicrobiology Journal* 23, no. 3–4 (2006): 213–226, https://doi.org/10.1080/01490450600724233.

47. A. Ebigbo, A. Phillips, R. Gerlach, et al., "Darcy-Scale Modeling of Microbially Induced Carbonate Mineral Precipitation in Sand Columns," *Water Resources Research* 48, no. 7 (2012): W07519, https://doi.org/10.1029/2011WR011714.

48. B. G. O. Ribeiro and M. G. Gomez, "Dissolution Behavior of Ureolytic Biocementation: Physical Experiments and Reactive Transport Modeling," *Journal of Geotechnical and Geoenvironmental Engineering* 149, no. 9 (2023): 04023071, https://doi.org/10.1061/jggefk.Gteng-11275.

49. L. N. Plummer and E. Busenberg, "The Solubilities of Calcite, Aragonite and Vaterite in CO_2-H_2O Solutions Between 0 and 90°C, and an Evaluation of the Aqueous Model for the System $CaCO_3$-CO_2-H_2O," *Geochimica et Cosmochimica Acta* 46, no. 6 (1982): 1011–1040, https://doi.org/10.1016/0016-7037(82)90056-4.

50. M. O. Cuthbert, M. S. Riley, S. Handley-Sidhu, et al., "Controls on the Rate of Ureolysis and the Morphology of Carbonate Precipitated by *S. pasteurii* Biofilms and Limits due to Bacterial Encapsulation," *Ecological Engineering* 41 (2012): 32–40, https://doi.org/10.1016/j.ecoleng.2012.01.008.

51. G. El Mountassir, R. J. Lunn, H. Moir, and E. MacLachlan, "Hydrodynamic Coupling in Microbially Mediated Fracture Mineralization: Formation of Self-Organized Groundwater Flow Channels," *Water Resources Research* 50, no. 1 (2014): 1–16, https://doi.org/10.1002/2013wr013578.

52. F. Weinhardt, H. Class, S. V. Dastjerdi, N. Karadimitriou, D. Lee, and H. Steeb, "Experimental Methods and Imaging for Enzymatically Induced Calcite Precipitation in a Microfluidic Cell," *Water Resources Research* 57, no. 3 (2021): e2020WR029361, https://doi.org/10.1029/2020WR029361.

53. Y. Wang, K. Soga, J. T. Dejong, and A. J. Kabla, "A Microfluidic Chip and Its Use in Characterising the Particle-Scale Behaviour of Microbial-Induced Calcium Carbonate Precipitation (MICP)," *Géotechnique* 69, no. 12 (2019): 1086–1094, https://doi.org/10.1680/jgeot.18.P.031.

54. V. S. Whiffin, L. A. van Paassen, and M. P. Harkes, "Microbial Carbonate Precipitation as a Soil Improvement Technique," *Geomicrobiology Journal* 24, no. 5 (2007): 417–423, https://doi.org/10.1080/01490450701436505.

55. J. P. Walsh, D. R. Corbett, J. M. Kiker, A. R. Orpin, R. P. Hale, and A. S. Ogston, "Spatial and Temporal Variability in Sediment Deposition and Seabed Character on the Waipaoa River Margin, New Zealand," *Continental Shelf Research* 86 (2014): 85–102, https://doi.org/10.1016/j.csr.2014.07.001.

56. L. Zhang, Z. Zhang, Y. Chen, and Y. Fu, "Sediment Characteristics, Floods, and Heavy Metal Pollution Recorded in an Overbank Core From the Lower Reaches of the Yangtze River," *Environmental Earth Sciences* 74, no. 11 (2015): 7451–7465, https://doi.org/10.1007/s12665-015-4733-8.

57. Y. Yang, M. Rogowska, Y. Zheng, et al., "Transient Increase in Reactive Surface and the Macroscopic Damköhler Number in Chalk Dissolution," *Journal of Hydrology* 571 (2019): 21–35, https://doi.org/10.1016/j.jhydrol.2019.01.032.

58. M. Liu and P. Mostaghimi, "Reactive Transport Modelling in Dual Porosity media," *Chemical Engineering Science* 190 (2018): 436–442, https://doi.org/10.1016/j.ces.2018.06.005.

59. K.-Q. Li, Z.-Y. Yin, and Y. Liu, "Influences of Spatial Variability of Hydrothermal Properties on the Freezing Process in Artificial Ground Freezing Technique," *Computers and Geotechnics* 159 (2023): 105448, https://doi.org/10.1016/j.compgeo.2023.105448.